

1 **Mixing layer height on the North China Plain and meteorological**
2 **evidence of serious air pollution in southern Hebei**

3 Xiaowan Zhu^{1,2}, Guiqian Tang^{1*}, Jianping Guo³, Bo Hu¹, Tao Song¹, Lili Wang¹,
4 Jinyuan Xin¹, Wenkang Gao¹, Christoph Münkel⁴, Klaus Schäfer⁵, Xin Li^{1,6}, and
5 Yuesi Wang¹

6

7 ¹State Key Laboratory of Atmospheric Boundary Layer Physics and Atmospheric
8 Chemistry (LAPC), Institute of Atmospheric Physics, Chinese Academy of Sciences,
9 Beijing 100029, China

10 ²University of Chinese Academy of Sciences, Beijing 10049, China

11 ³State Key Laboratory of Severe Weather & Key Laboratory of Atmospheric
12 Chemistry of CMA, Chinese Academy of Meteorological Sciences, Beijing 100081,
13 China

14 ⁴Vaisala GmbH, 22607 Hamburg, Germany

15 ⁵Atmospheric Science College, Chengdu University of Information Technology
16 (CIUT), Chengdu 610225, China

17 ⁶Beijing Municipal Committee of China Association for Promoting Democracy,
18 Beijing 100035, China

19

20 *Correspondence to:* G. Tang (tqq@dq.cern.ac.cn)

21

22 **Abstract**

23 To investigate the spatiotemporal variability of the mixing layer height (MLH) on the
24 North China Plain (NCP), multi-site and long-term observations of the MLH with
25 ceilometers at three inland stations (Beijing (BJ), Shijiazhuang (SJZ) and Tianjin (TJ))
26 and one coastal site (Qinhuangdao) were conducted from 16 October 2013 to 15 July
27 2015. The MLH of the inland stations in the NCP were highest in summer and lowest
28 in winter, while the MLH on the coastal area of Bohai was lowest in summer and
29 highest in spring. As a typical site in southern Hebei, the annual mean of the MLH at
30 SJZ was 464 ± 183 m, which was 15.0 % and 21.9 % lower than that at the BJ
31 (594 ± 183 m) and TJ (546 ± 197 m) stations, respectively. Investigation of the shear
32 term and buoyancy term in the NCP revealed that these two parameters in southern
33 Hebei were 2.8 times lower and 1.5 times higher than that in northern NCP within
34 0-1200 m in winter, respectively, leading to a 1.9-fold higher frequency of the
35 Gradient Richardson number >1 in southern Hebei compared to the northern NCP.
36 Furthermore, combined with aerosol optical depth and PM_{2.5} observations, we found
37 that the pollutant column concentration contrast (1.2 times) between these two areas
38 was far less than the near-ground PM_{2.5} concentration contrast (1.5 times). Through
39 analysis of the ventilation coefficient in the NCP, the near-ground heavy pollution in
40 southern Hebei mainly resulted from the lower MLH and wind speed. Therefore, due
41 to the importance of unfavorable weather conditions, heavily polluting enterprises
42 should be relocated and strong emission reduction measures are required to improve

43 the air quality in southern Hebei.

44 1. Introduction

45 The convective boundary layer is the region where turbulence is fully developed.
46 The height of the interface where turbulence is discontinuous is usually referred to as
47 the mixing layer height (MLH) (Stull, 1988). The mixing layer is regarded as the link
48 between the near-surface and free atmosphere, and the MLH is one of the major
49 factors affecting the atmospheric dissipation ability, which determines both the
50 volume into which ground-emitted pollutants can disperse, as well as the convective
51 time scales within the mixing layer (Seidel et al., 2010). In addition, continuous MLH
52 observations will be of great importance for the improvement of boundary layer
53 parameterization schemes and for the promotion of meteorological model accuracy.

54 Conventionally, the MLH is usually estimated from radiosonde profiles (Seidel et
55 al., 2010). Although meteorological radiosonde observations can provide high-quality
56 data, they are not suitable for continuous fine-resolution MLH retrievals due to their
57 high cost and limited observation intervals (Seibert et al., 2000). As the most
58 advanced method of MLH detection, remote sensing techniques based on the profile
59 measurements from ground-based instruments such as sodar, radar, or lidar that have
60 the unique vertically resolved observational capability are becoming increasingly
61 popular (Beyrich, 1997; Chen et al., 2001; He et al., 2005). Because sound waves can
62 be easily attenuated in the atmosphere, the vertical range of sodar is generally limited
63 to within 1000 m. However, the optical remote sensing techniques can provide higher
64 height ranges (at least several kilometers). The single-lens ceilometers developed by
65 Vaisala have been widely used in a variety of MLH studies (Alexander et al., 2017;
66 Emeis et al., 2004, 2009, 2011; Eresmaa et al., 2006; Münkel et al., 2004, 2007;
67 Muñoz and Undurraga, 2010; Schween et al., 2014; Sokół et al., 2014; Tang et al.,
68 2015, 2016; Wagner et al., 2006, 2015). Compared with other remote sensing
69 instruments, this type of lidar has special features favorable for long-term and
70 multi-station observations (Emeis et al., 2009; Wiegner et al., 2014; Tang et al., 2016),
71 including the low-power system, the eye-safe operation within a near infrared laser
72 band, and the low cost and ease of maintenance during any weather conditions
73 (excluding rainy, strong windy or sandstorm weather conditions) with only regular
74 window cleaning required (Emeis et al., 2004; Tang et al., 2016).

75 The North China Plain (NCP) region is the political, economic and cultural center
76 of China. With the rapid economic development, energy use has increased
77 substantially, resulting in frequent air pollution episodes (Guo et al., 2011; Li et al.,
78 2013; Liu et al., 2016; Tang et al., 2017b; Wang et al., 2014; Wang et al., 2013a; Xu et
79 al., 2016; Zhang et al., 2014). The haze pollution has had an adverse impact on human
80 health (Tang et al., 2017a) and has aroused a great deal of concern (Tang et al., 2009;
81 Ji et al., 2012; Zhang et al., 2015a). To achieve the integrated development of the
82 Jing-Jin-Ji region, readjustment of the regional industrial structure and layout is
83 imperative. To this end, the industrial capacity of heavily polluting enterprises in the
84 areas with unfavorable weather conditions should be reduced, and these heavily
85 polluting enterprises should be removed to improve the air quality. For the remaining
86 enterprises, the industrial air pollutant emissions structure should be changed, and

87 strong emission reduction measures must be implemented. Although the government
88 has carried out some strategies for joint prevention and control, with the less
89 well-understood distributions of regional weather condition on the NCP, how and
90 where to adjust the industrial structures on the NCP are questions in pressing need of
91 answers. As one of the key factors influencing the regional heavy haze pollution
92 (Tang et al., 2012, 2016, 2017b; Quan et al., 2013; Hu et al., 2014; Zhu et al., 2016;
93 Zhang et al., 2016a), the MLH to some extent represents the atmospheric
94 environmental capacity, and the regional distribution and variation of MLH on the
95 NCP can offer a scientific basis for regional industrial distribution readjustment,
96 which will be of great importance for regional haze management.

97 Nevertheless, due to the scarcity of MLH observations on the NCP, reliable and
98 explicit characteristics of MLH on the NCP remain unknown. Tang et al. (2016)
99 utilized the long-term observation data of MLH from ceilometers to analyze the
100 characteristics of MLH variations in Beijing (BJ) and verified the reliability of
101 ceilometers. The results demonstrated that MLH in BJ was high in spring and summer
102 and low in autumn and winter with two transition months in February and September.
103 A multi-station analysis of MLH on the NCP region was conducted in February 2014,
104 and the characteristics of high MLH at coastal stations and low MLH at southwest
105 piedmont stations were reported (Li et al., 2015). Miao et al. (2015) modeled the
106 seasonal variations of MLH on the NCP and discovered that the MLH was high in
107 spring due to the strong mechanical forcing and low in winter as a result of the strong
108 thermodynamic stability in the near-surface layer. The mountain-plain breeze and the
109 sea breeze circulations played an important role in the mixing layer process when the
110 background synoptic patterns were weak in summer and autumn (Tang et al., 2016;
111 Wei et al., 2017).

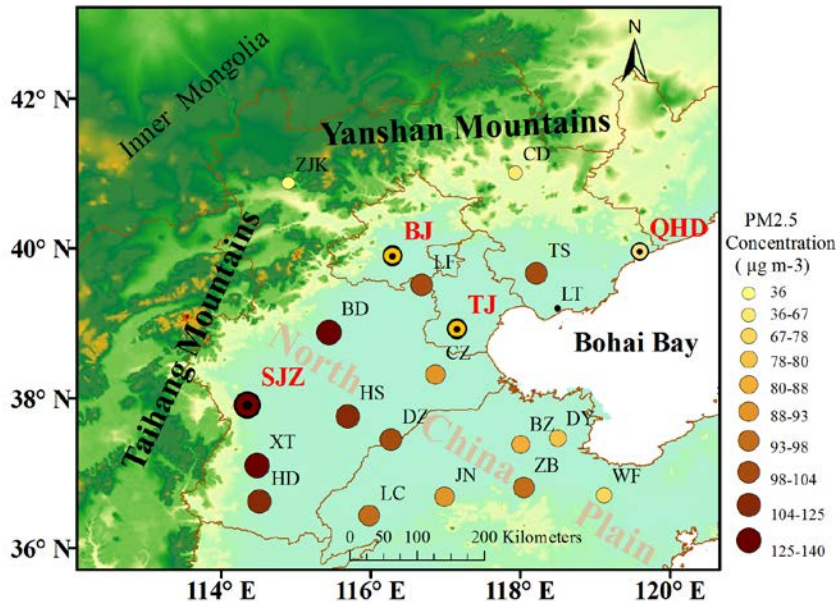
112 To overcome previous studies' deficiencies, our study first conducted a 22-month
113 (from 16 October 2013 to 15 July 2015) observation of MLH with ceilometers on the
114 NCP. The observation stations included three inland stations (BJ, Shijiazhuang (SJZ)
115 and Tianjin (TJ)) and one coastal site (Qinhuangdao (QHD)). First, we will describe
116 the spatial and temporal distribution of MLH on the NCP. Subsequently, reasons for
117 spatial difference of MLH on the NCP will be explained in the discussion section.
118 Finally, the meteorological evidence of serious air pollution in southern Hebei will be
119 studied.

120 **2 Data and methods**

121 **2.1 Sites**

122 To study the MLH characteristics on the NCP, observations with ceilometers were
123 conducted at the BJ, SJZ, TJ and QHD stations from 16 October 2013 to 15 July 2015
124 (Fig. 1 and Table S1). The SJZ, TJ and QHD sites were set around Beijing in the
125 southwest, southeast and east directions, respectively. The BJ station was at the base
126 of the Taihang and Yanshan Mountains on the northern NCP. The MLH observation
127 site was built in the courtyard of the Institute of Atmospheric Physics, Chinese
128 Academy of Sciences (116.32° E, 39.90° N). SJZ was near the Taihang Mountain in
129 southern Hebei; the location was in the Hebei University of Economics (114.26° E,
130 38.03° N). The TJ site was set in the courtyard of the Tianjin Meteorological Bureau,

131 which was located south of the urban area, with a geographic location of 117.20° E,
 132 39.13° N. The QHD station was an eastern coastal site of Bohai Bay, which was set
 133 up in the Environmental Management College of China (119.57° E, 39.95° N), and
 134 the surrounding areas are mostly residential buildings with no high structures. Since
 135 the TJ site was approximately 50 km away from the coast and the QHD station was
 136 only 2 km, the TJ station, by contrast, was supposed to be an inland station.



137
 138 Fig. 1 Locations of the ceilometers observation sites (BJ, SJZ, TJ and QHD) are
 139 marked with red and bold abbreviations; other PM_{2.5} observation sites (ZJK, CD, LF,
 140 TS, CZ, BD, HS, XT, HD, DZ, LC, JN, BZ, DY, ZB and WF) and the sounding
 141 observation sites (BJ, LT and XT) are marked on the map with black abbreviations.
 142 The size and color of the circular mark are representative of the annual mean
 143 near-ground PM_{2.5} concentration; the larger and darker the circle is, the greater the
 144 concentration is.

145 2.2 Measurement of MLH

146 The instrument used to measure the MLH at the four stations was an enhanced
 147 single-lens ceilometer (Vaisala, Finland), which utilized the strobe laser lidar (laser
 148 detection and range measurement) technique (910 nm) to measure the attenuated
 149 backscattering coefficient profiles. As large differences existed in the aerosol
 150 concentrations between the mixing layer and the free atmosphere, the MLH can be
 151 determined from the vertical attenuated backscattering coefficient (β) gradient,
 152 whereby a strong, sudden change in the negative gradient ($-d\beta/dx$) can indicate the
 153 MLH. In the present study, the Vaisala software product BL-VIEW was utilized to
 154 calculate the MLH by determining the location of the maximum $|-d\beta/dx|$ in the
 155 attenuated backscattering coefficient. To strengthen the echo signals and reduce the
 156 detection noise, spatial and temporal averaging should be conducted before the
 157 gradient method is used to calculate the MLH. The BL-VIEW software was utilized
 158 with temporal smoothing of 1200 s and vertical distance smoothing of 240 m. The
 159 instrument installed at the BJ station was a CL31 ceilometer and the CL51

160 ceilometers were used at the SJZ, TJ and QHD stations. Some of the properties of
161 these two instruments are listed in Table 1, and basic technical descriptions can be
162 found in Münkel et al. (2007) and Tang et al. (2015).

163 To ensure the consistency of the MLH measurements with the two different
164 ceilometer versions, before we set up the ceilometer observation network in the NCP,
165 we made a comparison of the MLHs observed by CL31 and CL51 at BJ from October
166 1 to October 8, 2013 (Fig. S1). The MLH observed by CL31 was highly relevant to
167 those observed by the CL51 ceilometers, with correlation coefficients (R) of 0.86-0.92.
168 Therefore, the impact of version discrepancy on the MLH measurement can be
169 neglected.

170 Since the ceilometers can reflect rainy conditions and the precipitation will
171 influence the MLH retrieval, the precipitation data were excluded. In addition, a
172 previous study has compared MLH measurements retrieved from ceilometers and
173 sounding data (Tang et al., 2016). The results revealed that the ceilometers
174 underestimate the MLH under neutral conditions caused by strong winds and
175 overestimate the MLH when sand storms occur. Therefore, data points for these three
176 special weather conditions were eliminated manually. The criterion to exclude these
177 data points is as follows: (a) precipitation, i.e., a cloud base lower than 4000 m and
178 the attenuated backscattering coefficient of at least $2 \times 10^{-6} \text{ m}^{-1} \text{ sr}^{-1}$ within 0 m and the
179 cloud base, (b) sandstorm, i.e., the ratio of $\text{PM}_{2.5}$ to PM_{10} suddenly decreased to 30 %
180 or lower and the PM_{10} concentration was higher than $500 \mu\text{g m}^{-3}$, and (c) strong winds,
181 i.e., a sudden change in temperature and wind speed (WS) when cold fronts passed by
182 (Muñoz and Undurraga, 2010; Tang et al., 2016; Van der Kamp and McKendry,
183 2010).

184 Table 1 Instrument properties of CL31 and CL51

Parameter	CL31	CL51
Detection range (km)	7.7	13.0
Wavelength (nm)	910	910
Report period (s)	2-120	6-120
Report accuracy (m)	5	10
Peak power (W)	310	310

185 **2.3 Other data**

186 The hourly data of near-ground relative humidity (RH) and temperature (T) in the
187 NCP region were obtained from the China Meteorological Administration
188 (<http://www.weather.com.cn/weather/101010100.shtml>). To study the reason for the
189 MLH difference between the northern NCP and southern Hebei, meteorological
190 sounding data were included in this paper. The data were provided by the upgraded
191 radiosonde network of China, where the GTS1 digital electronic radiosonde was
192 required to be operationally launched twice per day at 08:00 LT and 20:00 LT by the
193 China Meteorological Administration (Guo et al., 2016). Considering the deficiency
194 of sounding data at the SJZ and QHD stations, data from the Xingtai (XT) and
195 Laoting (LT) stations were used instead after a consistency test with the reanalysis
196 data (Fig. S2). The reanalysis data at these four sites were downloaded from the
197 website of European Centre for Medium-Range Weather Forecasts

198 (<http://apps.ecmwf.int/datasets/data/interim-full-mnths/levtype=pl/>).

199 The near-ground PM_{2.5} and PM₁₀ concentrations at the 20 observation sites from
200 December 2013 to November 2014 were provided by the Ministry of Environmental
201 Protection with a time resolution of 1 h (<http://www.zhb.gov.cn/>). Details for the
202 near-ground PM_{2.5} and PM₁₀ observation sites are shown in Table S1 and Fig. 1.

203 The aerosol optical depth (AOD) data within the NCP region were retrieved with
204 the dark target algorithm from the Moderate Resolution Imaging Spectra-radiometer
205 aerosol products on board the National Aeronautics and Space Administration Earth
206 Observing System Terra satellite from December 2013 to November 2014 (Zhang et
207 al., 2016b) (<https://ladsweb.nascom.nasa.gov/search/index.html>), then the AOD data
208 was interpolated into 0.1°×0.1° to produce the regional distribution in the NCP.

209 **2.4 Atmospheric stability criterion**

210 The Gradient Richardson number (*Ri*) is usually used to estimate the atmospheric
211 turbulent stability within the mixing layer and is defined as follows (Eq. 1):

$$212 \quad Ri = \frac{\frac{g \Delta \bar{\theta}}{\bar{\theta} \Delta z}}{\left(\frac{\Delta \bar{u}}{\Delta z}\right)^2 + \left(\frac{\Delta \bar{v}}{\Delta z}\right)^2} \quad (1)$$

213 Where Δz is the height increment over which a specific calculation of *Ri* is being
214 made; g is the acceleration of gravity; $\bar{\theta}$ is the mean virtual potential temperature
215 within that height increment; and $\Delta \bar{u}$ and $\Delta \bar{v}$ are the mean wind speeds in zonal and
216 meridional directions within the height increment.

217 Using *Ri* to diagnose turbulence is a classical approach and has been covered in
218 many textbooks on boundary-layer turbulence (Stull, 1988; Garratt, 1994). It can be
219 interpreted as the ratio of the buoyancy term ($\frac{g \Delta \bar{\theta}}{\bar{\theta} \Delta z}$) to the shear term ($\left(\frac{\Delta \bar{u}}{\Delta z}\right)^2 +$
220 $\left(\frac{\Delta \bar{v}}{\Delta z}\right)^2$) in the turbulent kinetic equation. When the *Ri*>1, the turbulence was
221 suppressed and the mixing layer development will be restrained (Stull, 1988). In our
222 study, the frequency of *Ri*>1 was used to represent the atmospheric stability in the
223 NCP. The larger the frequency is, the more stable turbulent stratification is.

224 **3. Results**

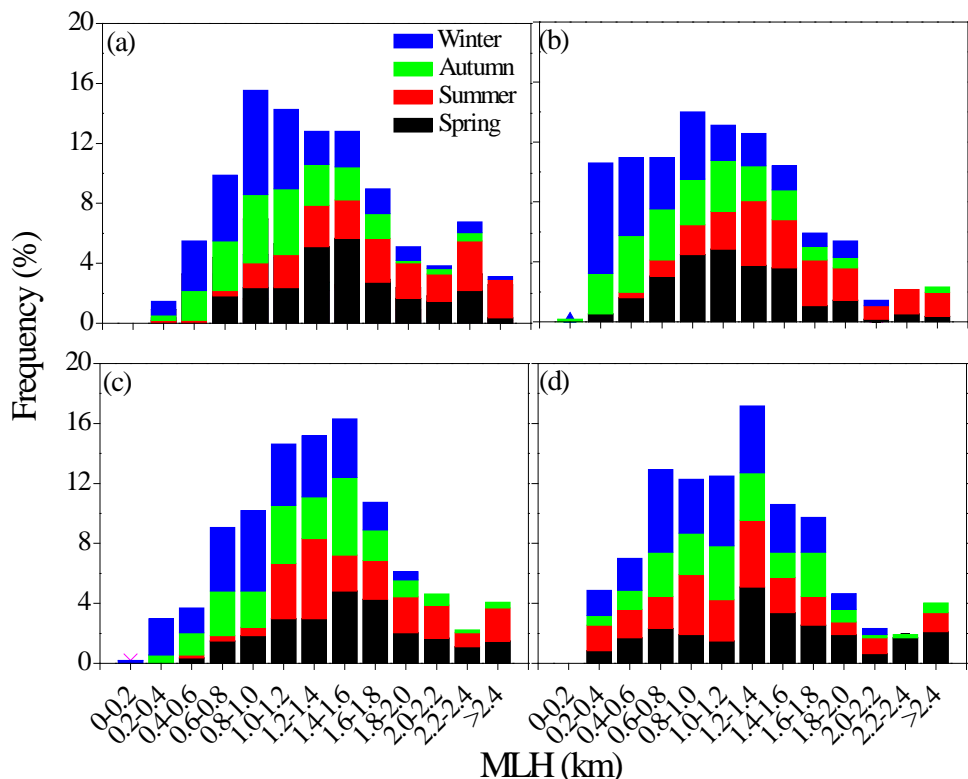
225 **3.1 Frequency distribution of MLH**

226 Since October 2013, continuous operation of the ceilometers observation network
227 in the NCP has provided 22 months of MLH data. For the purpose of analyzing the
228 MLH temporal and spatial variation, the hourly averages of MLH for a whole year
229 (from December 2013 to November 2014) at the BJ, SJZ, TJ and QHD stations were
230 chosen in the following sections. Hourly means of MLH under rainy, sandstorm and
231 windy conditions were removed, resulting in data availability of 81, 89, 83 and 77 %
232 at the BJ, SJZ, TJ and QHD stations, respectively. In this study, March, April and May
233 are defined as spring; June, July and August are defined as summer; September,
234 October and November are defined as autumn; and December, January and February
235 are defined as winter.

236 To study the regional distribution characteristic of MLH on the NCP, we analyzed
237 the frequency of the daily maximum MLH distribution in Fig. 2. The daily maximum

238 MLH at the BJ, SJZ and TJ stations could reach 2400 m. The large daily maximum
 239 values mostly existed in spring and summer, while the low values always appeared in
 240 autumn and winter and were as low as 200 m. The daily maximum MLH values at the
 241 BJ, SJZ and TJ stations were mainly distributed between 600 and 1800 m, 400 and
 242 1600 m and 800 and 1800 m, accounting for 74.2, 72.0 and 67.0 % of the total
 243 samples, respectively. Notably, the daily maximum MLH in SJZ was lower than at the
 244 MLHs at the BJ and TJ stations in spring, autumn and winter. Values below 600 m at
 245 the SJZ station occurred primarily in autumn and winter. The most frequent daily
 246 maximum MLH existed in the range of 1000-1200 m, which was 200-600 m lower
 247 than that at the TJ station. This demonstrated a weaker atmospheric diffusion
 248 capability at the SJZ station in spring, autumn and winter than the northern NCP
 249 stations.

250 The frequency distribution of the daily maximum MLH at the coastal site showed
 251 different features. The daily maximum MLH in QHD was mainly distributed between
 252 800 and 1800 m with a relatively small seasonal fluctuation (Fig. 2d). Values lower
 253 than 600 m were mainly distributed in summer, which was probably influenced by the
 254 frequent occurrence of a thermal internal boundary layer (TIBL) in summer. Reasons
 255 for this are illustrated in section 4.1.



256
 257 Fig. 2 Frequency distribution of the daily maximum MLH at the (a) BJ, (b) SJZ, (c)
 258 TJ and (d) QHD stations from December 2013 to November 2014.

259 3.2 Spatiotemporal variation of MLH

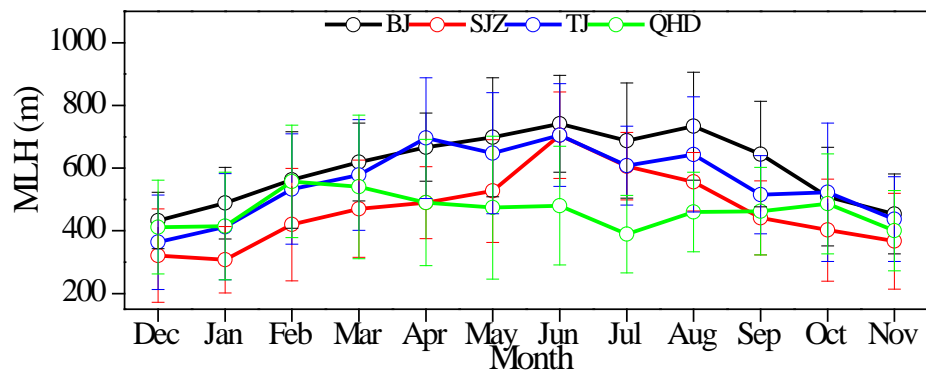
260 3.2.1 Seasonal variation

261 Monthly variations of MLH at the BJ, SJZ, TJ and QHD stations are shown in Fig.
 262 3. The monthly means of the regional MLH ranged between 300 and 750 m. The
 263 maximum and minimum MLH existed in June 2014 at the BJ station and in January

264 2014 at the SJZ station, with values of 741 and 308 m, respectively. Most of the
 265 monthly averages were between 400 and 700 m, which accounted for 81.3 % of the
 266 total samples.

267 The MLH at the BJ, SJZ and TJ stations showed obvious seasonal variations with
 268 high values in spring and summer and low values in autumn and winter. Seasonal
 269 means of MLH at the three stations followed the same order: summer>spring>autumn>winter, with maximum values of 722 ± 169 , 623 ± 161 and
 270 655 ± 165 m in summer, respectively, and minimum values of 493 ± 131 , 347 ± 153 and
 271 436 ± 178 m in winter, respectively (Table S2). Obvious annual changes of the MLH
 272 with large values in spring and summer and low values in autumn and winter at the BJ,
 273 SJZ and TJ stations implied that MLH is influenced by seasonal changes of solar
 274 radiation (Stull, 1988).

275 Nevertheless, the seasonal variation of MLH at the coastal site of Bohai was
 276 different from that at the inland stations. The MLH in QHD exhibited a decreasing
 277 trend from spring to summer and an increasing trend from autumn to winter, with the
 278 maximum seasonal mean of 498 ± 217 m in spring and the minimum seasonal mean of
 279 447 ± 153 m in summer. Moreover, the MLH in spring and summer at QHD was much
 280 lower than those at other stations. Similar to our analysis of frequency distributions of
 281 daily maximum MLH in section 3.1, the lower MLH at QHD in spring and summer
 282 mainly resulted from the frequent occurrence of the TIBL. A detailed explanation of
 283 the TIBL impact was included in section 4.1. The effect of TIBL on the coastal
 284 boundary layer was consistent with previous studies (Zhang et al., 2013; Tu et al.,
 285 2012), which demonstrated that ceilometers can properly retrieve the coastal MLH as
 286 well.
 287



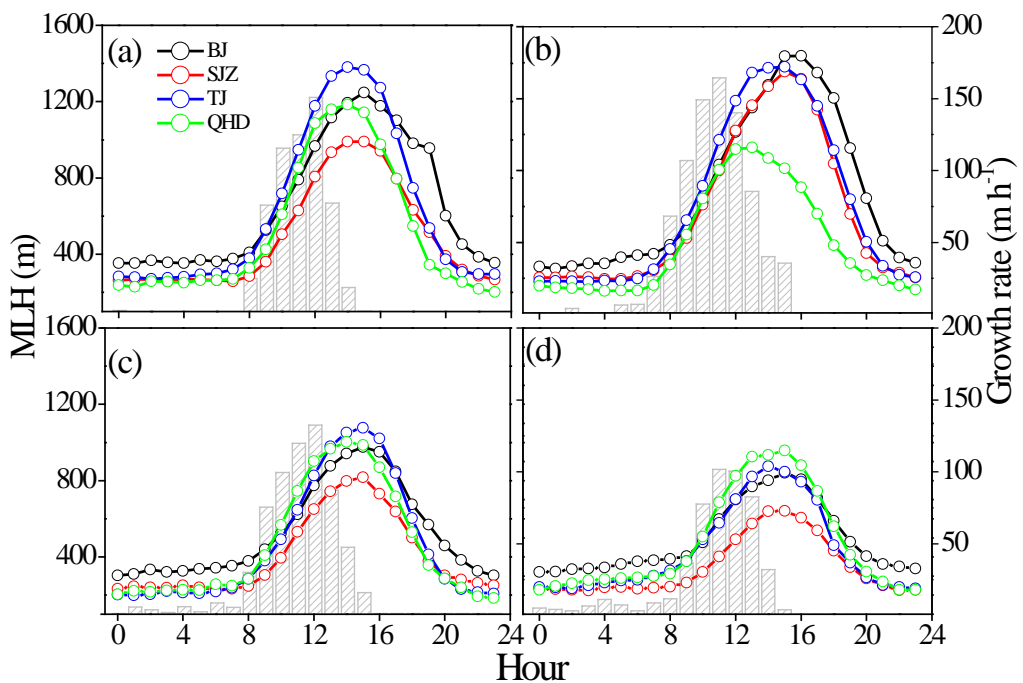
288
 289 Fig. 3 Monthly variations of MLH at the BJ, SJZ, TJ and QHD stations from
 290 December 2013 to November 2014.

291 3.2.2 Diurnal variations

292 Seasonal variations of diurnal MLH change patterns were investigated to reveal the
 293 24 h evolution characteristics of the MLH on the NCP. As shown in Fig. 4, diurnal
 294 variations of MLH in different seasons all had single peak patterns. With sunrise and
 295 increased solar radiation, MLH at the four stations started to develop and peaked in
 296 the early afternoon. After sunset, turbulence in the MLH decayed quickly, and the
 297 mixing layer underwent a transition to the nocturnal stable layer (less than 400 m).
 298 The annual averaged diurnal ranges of MLH at the BJ, SJZ, TJ and QHD stations

were 782, 699, 914 and 790 m, respectively. The annual averaged diurnal range of MLH in SJZ was approximately 100-200 m smaller than those at the other stations, which was associated with its shallow daytime MLHs in spring, autumn and winter (Figs. 4a, 4c and 4d). This also indicated the worse pollutant diffusion ability in SJZ.

Growth rates averaged over the four stations during each season were plotted with gray columns in Fig. 4. It was obvious that the growth rates of the MLH varied by season. The MLH developed the earliest in summer (at approximately 7:00 LT) and reached the highest growth rates (164.5 m h^{-1}) at approximately 11:00 LT, and the time when MLH started to develop was found to be 1 hour later (at approximately 8:00 LT) in spring and autumn than in summer. Furthermore, the MLH developed the latest (at approximately 9:00 LT) and slowest in winter, with the maximum growth rate (101.8 m h^{-1}) occurring at approximately 11:00 LT.



311
312 Fig. 4 Diurnal variations of MLH at the BJ, SJZ, TJ and QHD stations in (a) spring, (b)
313 summer, (c) autumn and (d) winter seasons are indicated by lines and scatters. The
314 growth rates averaged over the four sites are drawn with gray columns for each season
315 to represent the MLH growth velocity, and only positive values are shown in the
316 figure.

317 Annual averages of MLH at the BJ, SJZ, TJ and QHD stations were also calculated,
318 and the values were 594 ± 183 , 464 ± 183 , 546 ± 197 and 465 ± 175 m, respectively. The
319 MLH at SJZ was approximately 21.9, 15.0 and 0.2 % lower than at the BJ, TJ and
320 QHD stations, respectively. Therefore, according to the analysis above in sections 3.1
321 and 3.2, an obvious phenomenon can be observed in the MLH distribution on the
322 NCP: the MLH in southern Hebei was lower than in the northern NCP in spring,
323 autumn and winter but was almost equal to the northern areas in summer.

324 4. Discussion

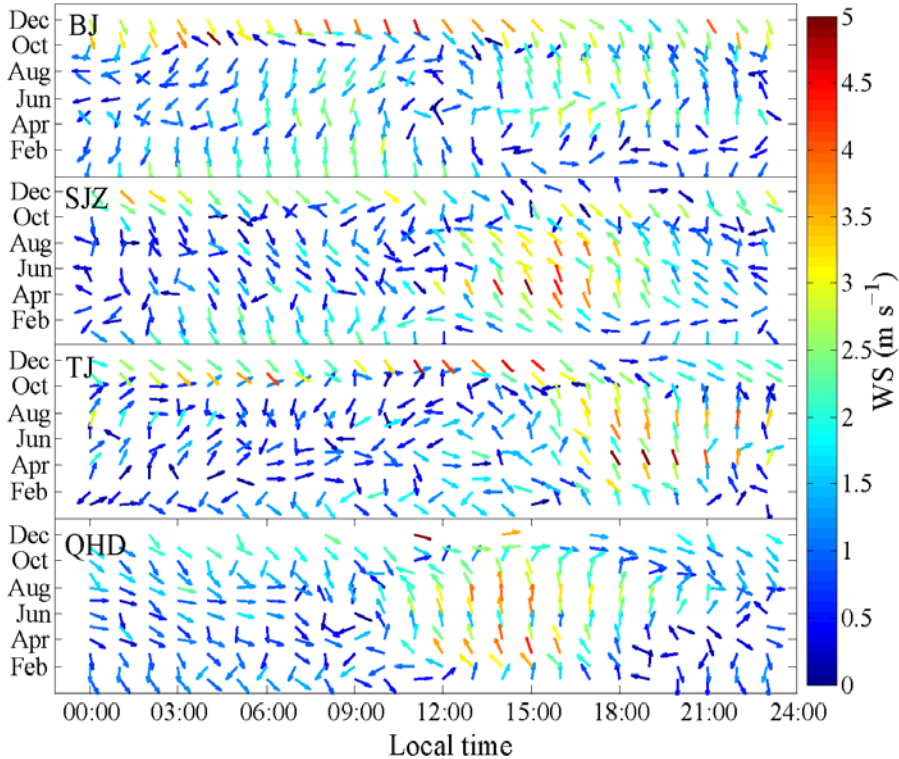
325 Through preliminary study of the spatiotemporal variation of MLH on the NCP
326 region, we found something interesting: (a) the MLH at the coastal site was lower

327 than the inland sites in summer; (b) the MLH in southern Hebei was lower than the
328 northern NCP in spring, autumn and winter, but was almost consistent between these
329 two areas in summer. Reasons for these two phenomena will be illustrated in the
330 following sections (4.1 and 4.2). Finally, we will investigate the meteorological
331 evidence for serious haze pollution in southern Hebei in section 4.3.

332 **4.1 The TIBL impact in coastal site**

333 From the studies in sections 3.1 and 3.2, we found that the maximum MLH at the
334 QHD station was larger and arrived earlier than the BJ, SJZ and TJ stations in summer
335 (Fig. 4b). However, this characteristic was not evident in other seasons (Figs. 4a, 4c
336 and 4d). The sea-land breeze was a local circulation that occurs when there is no
337 large-scale synoptic system passes. In our study, we first excluded days with
338 large-scale synoptic systems. Then, according to the coastline orientation, if the
339 southeast wind at the TJ station and south and southwest winds at the QHD station
340 occurred at approximately 11:00 LT, and the northwest wind started to blow at
341 approximately 20:00 LT, then this type of circulation was supposed to be a sea-land
342 circulation. The prevailing southeast wind at the TJ station and the south and
343 southwest wind at the QHD station were regarded as sea breezes (Fig. 5).

344 The sea breeze usually brings a cold and stable air mass from the sea to the coastal
345 region. When the top of the local mixing layer was higher than the top of the air mass,
346 a TIBL will develop within the mixing layer under the influence of the abrupt change
347 of aerodynamic roughness and temperature between the land and sea surfaces. Then,
348 the local mixing layer will be replaced by the TIBL. In the presence of warm air on
349 land, the cold sea air advects downwind and is warmed, leading to a weak temperature
350 difference between the air and the ground. In consequence, the TIBL warms less
351 rapidly due to the decreased heat flux at the ground, and the rise rate is reduced. In
352 addition, since the TIBL deepens with distance downwind and usually can not extend
353 all the way to the top of the intruding marine air, the remaining cool marine air above
354 the TIBL will hinder vertical development of the TIBL (Stull, 1988; Sicard et al.,
355 2006; Puygrenier et al., 2005; Tomasi et al., 2011). With distance inland, the top of
356 the intruding marine air will enhance and exceed the local MLH; if so, the TIBL will
357 not form, and the TIBL impact will be impaired with distance inland (Stull, 1988).
358 Accompanied by the weak synoptic system and the frequent occurrence of sea breezes
359 in summer, the TIBL formed easily and the MLH peak time and value at the QHD
360 station were earlier and lower than other stations (Figs. 3 and 4). For the TJ station,
361 with a distance of approximately 50 km out to sea, the TIBL will not extend so far.
362 Therefore, although the TJ station can be affected by the sea breeze, the local MLH
363 cannot be influenced by the TIBL.

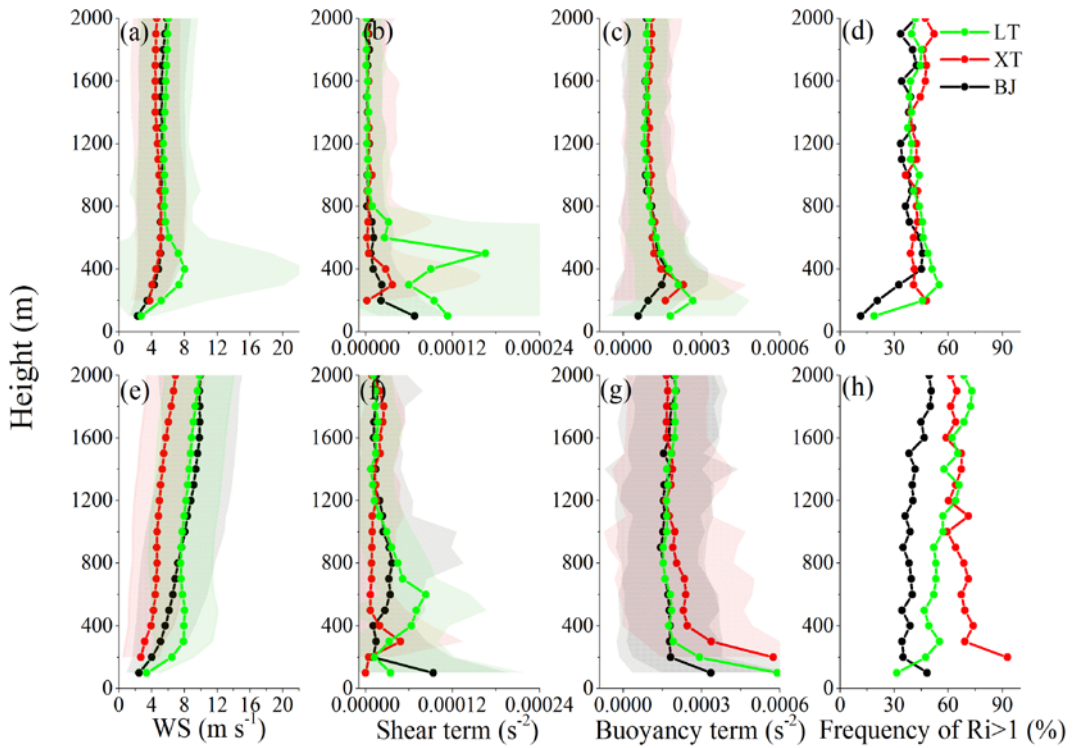


364

365 Fig. 5 Monthly diurnal wind vectors at the BJ, SJZ, TJ and QHD stations from
 366 December 2013 to November 2014.

367 4.2 Reasons for low MLH in southern Hebei

368 Turbulent stability was mainly responsible for the MLH development, and the
 369 generation of turbulent energy was highly correlated with the heat flux (mainly
 370 sensible heat fluxes) produced by radiation and the momentum flux caused by wind
 371 shear (Stull, 1988). As presented in section 2.4, the Ri could describe the turbulent
 372 stability not only from the perspective of thermal forces but also from the perspective
 373 of mechanical forces; it was calculated in this section with meteorological sounding
 374 profiles to study the reason for MLH differences between southern Hebei and the
 375 northern NCP, and the frequency values of $Ri > 1$ were given in this study. With larger
 376 frequency comes more stable stratification. Considering the geographic locations (Fig.
 377 1), the lack of sounding data at the SJZ station was replaced by sounding data from
 378 the XT station; meanwhile, sounding data from the LT station was used instead of the
 379 data from QHD. Each of the four parameter profiles (WS, shear term, buoyancy term,
 380 and the frequency of $Ri > 1$) at the BJ, XT and LT stations are depicted in Fig. 6. The
 381 profiles were averaged over 8:00 LT and 20:00 LT and vertically smoothed using a
 382 100-m running average to reduce unexpected fluctuations for viewing purposes only.



383

384 Fig. 6 Vertical profiles of (a, e) horizontal WS, (b, f) shear term, (c, g) buoyancy term
 385 and (d, h) frequency of $Ri>1$ at the BJ, XT and LT stations in summer (upper panel)
 386 and winter (lower panel).

387 Using the winter and summer as examples, when we analyzed the seasonal means
 388 of shear term and the buoyancy term between the XT and the BJ stations, some
 389 distinct features were observed. As shown in Figs. 6f and 6g, the shear term and the
 390 buoyancy term in XT was 2.8 times lower and 1.5 times higher than that in BJ within
 391 0-1200 m in winter, respectively. The largest discrepancies of the wind shear term and
 392 buoyancy term between southern Hebei and the northern NCP could reach 2.84×10^{-5}
 393 s^{-2} at the altitude of 800 m and $3.93 \times 10^{-4} s^{-2}$ at 200 m, respectively. As a result, the
 394 frequency of $Ri>1$ in XT was approximately 1.9 times larger than that in BJ within
 395 0-1200 m, leading to a much more stable stratification in southern Hebei (Fig. 6h).
 396 The shear term, buoyancy term and the frequency of $Ri>1$ in spring and autumn
 397 displayed similar characteristics to those in winter, and the averaged frequency of
 398 $Ri>1$ in southern Hebei was approximately 1.5 and 1.3 times larger than those in
 399 northern NCP in spring and autumn, respectively (Fig. S3). While in summer, the
 400 shear term, buoyancy term and the frequency of $Ri>1$ were almost the same between
 401 southern Hebei and the northern NCP (Figs. 6b, 6c and 6d).

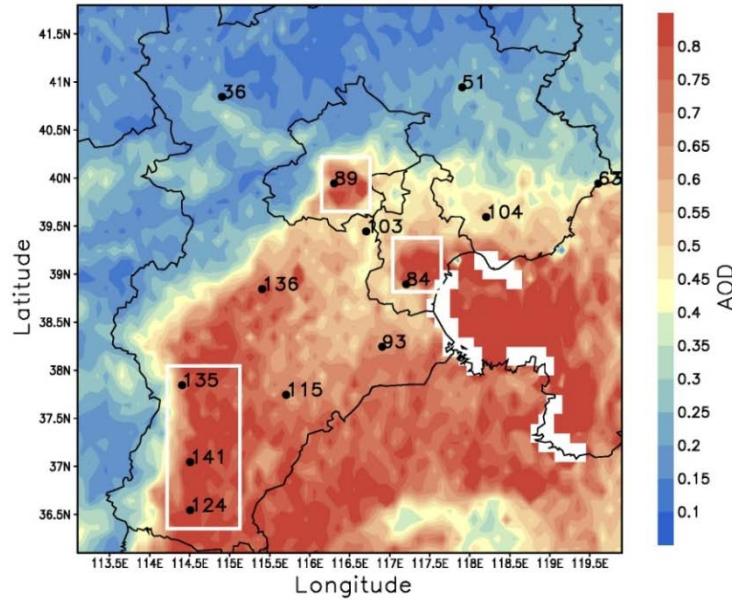
402 As a result, the lower MLH in southern Hebei was due to a more stable atmospheric
 403 turbulent structure than the northern NCP in spring, autumn and winter. This probably
 404 resulted from the frequent effect of cold air on the northern NCP, and such cold air
 405 was usually too weak to reach southern Hebei (Su et al., 2004). Then the cold front
 406 resulting from the cold air system will enhance the wind shear over the northern NCP.
 407 In addition, a previous study has revealed that the warm advection from the Loess
 408 Plateau usually developed from south to north, and the lower MLH in southern Hebei
 409 will be partially related to the enhance thermal inversion at the altitude of 1500 m (Hu

410 et al., 2014; Zhu et al., 2016). In summer, due to the northward lift and westward
411 intrusion of the subtropical high on the NCP, the diminishing existence of the weak
412 cold air on the northern NCP accompanied with the regional scale strong solar
413 radiation and strong turbulent activities will lead to a small turbulent stability contrast
414 between southern Hebei and the northern NCP.

415 In addition, other researchers proposed that absorbing aerosols above the MLH can
416 be another factor affecting the MLH (Peng et al., 2016; Wang et al., 2013; Li et al.,
417 2016). Absorbing aerosols gives rise to an increasing temperature aloft but a
418 decreasing temperature at the surface, which will enhance the strength of capping
419 inversion and inhibit the convective ability. In contrast, absorbing aerosols within the
420 mixing layer could reduce the capping inversion intensity despite the reduction in the
421 surface buoyancy flux and raise the MLH (Yu et al., 2002). Considering the higher
422 concentrations of surface $PM_{2.5}$ in southern Hebei, absorbing aerosols could have
423 some impacts on MLH development. However, the comprehensive influences from
424 the feedback of absorbing aerosols above and below the MLH are hard to explain
425 without sufficient knowledge of vertical variations in absorbing aerosols at the four
426 stations. Additionally, the mixed state and morphology of absorbing aerosols
427 dominant the absorption effects (Jacobson, 2001; Bond et al., 2013). Therefore,
428 without sufficient observation data, it is difficult to discuss the possible influences of
429 air pollution feedback on MLH development in this study. Elaborate experiments of
430 vertical profiles and the morphology of absorbing aerosols are needed in future
431 studies.

432 **4.3 Meteorological evidence of serious air pollution in southern Hebei**

433 When we analyzed the near-ground $PM_{2.5}$ and PM_{10} concentration distributions on
434 the NCP from December 2013 to November 2014, a unique phenomenon was found
435 and shown in Fig. 1 and Fig. S4. The annual means of near-ground $PM_{2.5}$
436 concentration in southern Hebei (SJZ, XT and HD) was $133.3 \mu g m^{-3}$ ($225.3 \mu g m^{-3}$
437 for the PM_{10} concentrations), while in the northern areas (BJ and TJ), it was $86.5 \mu g$
438 m^{-3} ($126.0 \mu g m^{-3}$ for the PM_{10} concentrations), and the difference in the near-ground
439 $PM_{2.5}$ concentration between the two areas can be as high as 1.5-fold (1.8-fold for the
440 PM_{10} concentrations). Since AOD represents the aerosol column concentration, it is a
441 much better indicator for the emissions difference than the $PM_{2.5}$. Additionally, the
442 averaged annual AOD in southern Hebei was only 1.2 times of that in the northern
443 NCP (Fig. 7). If the difference in AOD represents the emission discrepancy, the
444 remaining differences of $PM_{2.5}$ may be induced by the meteorology. In other words,
445 meteorological conditions may play an important role in heavier haze formation in
446 southern Hebei and the meteorological condition contrast between these two areas
447 contributed approximately 60% to the $PM_{2.5}$ concentration discrepancy.

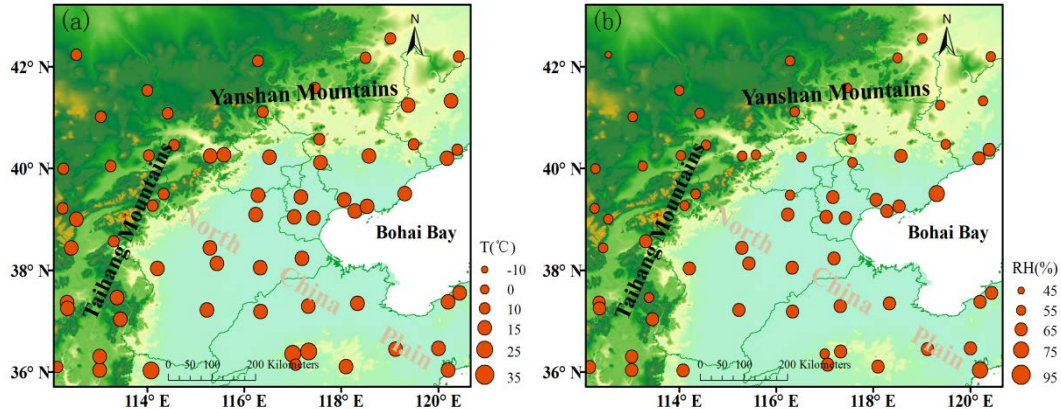


448
 449 Fig. 7 Distribution of the annual mean values of AOD from December 2013 to
 450 November 2014 in the NCP. The PM_{2.5} concentrations of the 13 observation sites
 451 were also marked beside each station. The major sites in the northern NCP (BJ and TJ)
 452 and southern Hebei (SJZ, XT and HD) are enclosed by white rectangles.

453 Previous studies revealed that the most significant meteorological factors for
 454 regional heavy haze formation in the NCP were RH and MLH (Tang et al., 2016; Zhu
 455 et al., 2016). In addition, the T influences the particles' physicochemical reaction rate
 456 and the ventilation coefficients (V_c) can be used as an index to evaluate the total
 457 diffusion ability of the atmosphere; thus, the RH, T and V_c were compared and
 458 analyzed among the four stations (BJ, SJZ, TJ and QHD) in the next section. The
 459 regional particle growth and the atmospheric dissipation ability will be discussed
 460 separately, each from a meteorological point of view.

461 **4.3.1 Meteorological factors for particle growth**

462 Distributions of annual means of T and RH are shown in Fig. 8, and the
 463 distributions of seasonal means of T and RH were added in Figs. S5 and S6. The T
 464 value in southern Hebei was similar to that on the northern NCP but was higher than
 465 that at the coastal site (Figs. 8a and S5). This indicated an almost consistent
 466 temperature condition for an atmospheric physicochemical reaction (Garratt et al.,
 467 1994; Zhang et al., 2010). However, differences existed in RH between southern
 468 Hebei and the northern NCP. The RH in the SJZ station was always higher than that in
 469 the BJ and TJ stations but was slightly lower than that at the coastal sites (Figs. 8b and
 470 S6). The annual averages of RH at the BJ, SJZ, TJ and QHD sites were 51.2, 65.7,
 471 57.0 and 68.6 %, respectively, and the RH at SJZ was 22.1 and 13.2 % higher than
 472 that at the BJ and TJ sites, respectively (Table S3). Since RH is a key factor for haze
 473 development, higher RH is beneficial to fine particle growth through hygroscopic
 474 growth processes and heterogeneous reactions (Zhao et al., 2013; Fu et al., 2014; Liu
 475 et al., 2011; Hu et al., 2006; Zhang et al., 2015; Seinfeld et al., 1998). Thus, a higher
 476 RH provided a favorable meteorological condition for haze development, which could
 477 be partially responsible for heavier pollution in southern Hebei.



478
479 Fig. 8 Distribution of annual means of (a) T and (b) RH in the NCP region from
480 December 2013 to November 2014.

481 4.3.2 Meteorological factors for particle dissipation

482 As MLH and WS can represent the atmospheric dissipation capability in the
483 vertical and horizontal directions, respectively, in addition to the MLH, we analyzed
484 the WS variations on the NCP. Similar to our analysis in section 4.2, as SJZ and QHD
485 had no sounding data and due to the close geographic proximity among SJZ and XT
486 as well as LT and QHD, sounding data from the XT and LT stations were used instead
487 of the data at SJZ and QHD, respectively. The WS profiles were averaged every 100
488 m at each station and are depicted in Figs. 6 and S3. Except for summer, the WS in
489 southern Hebei was far less than that on the northern NCP in spring, autumn and
490 winter (Figs. 6e, S3a and S3e) but was nearly consistent in summer (Fig. 6a). This
491 finding indicated a weaker horizontal diffusion capability in southern Hebei than that
492 on the northern NCP.

493 The V_c is an important factor in pollutant dissipation and air quality studies; it
494 accounts for the vertical dispersion and advection of pollutants. With a larger V_c ,
495 strong dissipation ability follows. The V_c is defined as the product of MLH and wind
496 transport (U_T) as shown in Eq. (2).

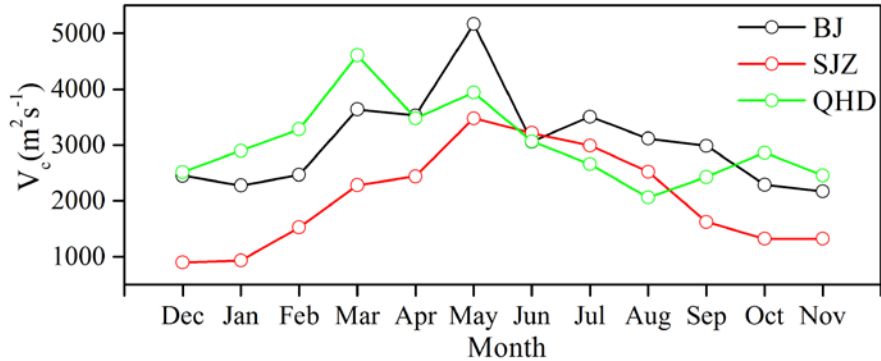
$$497 \quad V_c = \text{MLH} \times U_T \quad (2)$$

498 When we utilized the wind profiles in Figs. 6 and S3 with equal spacing in the vertical
499 direction, U_T could be regarded as the mean wind transport, i.e., $U_T = \frac{1}{n} \sum_{i=1}^n U_i$ where

500 U_i is the WS observed at each level and n is the number of levels within the mixing
501 layer (Nair et al., 2007). Since the WS was a climatic parameter, the WS profiles at
502 08:00 LT and 20:00 LT were used to approximate V_c approximately. Considering the
503 monthly averaged MLH at the BJ, SJZ and QHD stations, the monthly V_c were
504 depicted in Fig. 9. V_c at southern Hebei was always lower than that in the northern
505 NCP during the whole study period. The seasonal means of V_c at the BJ, SJZ and
506 QHD stations in spring, summer, autumn and winter were 4112.0, 2733.3 and 4008.5;
507 3227.5, 2908.8 and 2593.7; 2481.4, 1421.9 and 2581.7; and 2397.2, 1117.7 and
508 2900.0 $\text{m}^2 \text{s}^{-1}$, respectively. It was clear that the SJZ station usually had the lowest V_c ,
509 and the annual averaged V_c at SJZ was almost 1.5 and 1.5 times smaller than the BJ
510 and QHD stations, respectively (Table S3). As a result, the particle dissipation
511 capability in southern Hebei was much weaker than that in the northern NCP and

512 coastal areas.

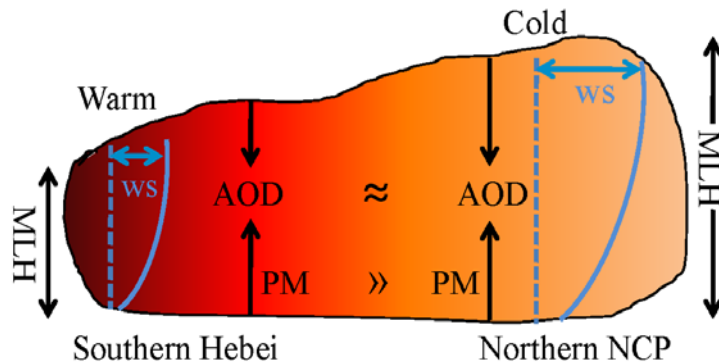
513



514

515 Fig. 9 Seasonal variations of V_c at the BJ, SJZ and QHD stations from December
516 2013 to November 2014. The V_c is defined as the product of MLH and wind transport
517 (Nair et al., 2007) (Eq. (2)). With a larger V_c , strong dissipation ability follows.

518 Therefore, with lower MLH, lower WS and higher RH occur in southern Hebei
519 compared to the northern NCP, the near-ground PM_{2.5} showed a large contrast
520 between these two areas. However, the AOD had little difference between southern
521 Hebei and the northern NCP. Apart from the emission contrast, the meteorological
522 condition contrast between these two areas heavily contributed to the heavy haze in
523 southern Hebei and the industrial structure is in need of readjustment for the NCP (Fig.
524 10).



525

526 Fig.10 The schematic diagram of the meteorological causes for heavy haze in
527 southern Hebei.

528 5. Conclusions

529 To gain new insight into the spatiotemporal variation of the regional MLH, the
530 present study conducted a simultaneous observation with ceilometers at three inland
531 stations (BJ, SJZ, and TJ) and one coastal site (QHD) to obtain high spatial and
532 temporal resolution MLH data. The experiment period lasted for 22-months from
533 October 16, 2013, to July 15, 2015, and a whole year of data (from December 2013 to
534 November 2014) were utilized for further study. Conclusions were drawn as follows.

535 The ceilometers can not only retrieve the inland MLH but also retrieve the coastal
536 MLH properly. The MLHs in the inland areas of the NCP were high in spring and
537 summer and low in autumn and winter. While under the impact of TIBL, the coastal

538 MLH had an opposite variation trend of inland sites and the lowest MLH in QHD
539 occurred in summer. The TIBL impaired the local MLH development at the coastal
540 site and caused the mixing layer to peak early in summer; this effect weakened with
541 distance inland.

542 The MLH in southern Hebei was lower than that on the northern NCP, especially in
543 spring, autumn and winter. This mainly resulted from the more stable turbulent
544 structure (weak shear term, higher buoyancy term and larger frequency of $Ri>1$) than
545 the northern NCP, and the stable stratification in southern Hebei was partially related
546 to the Siberian High and warm advection from the Loess Plateau. In summer, the
547 atmospheric stability was almost consistent between southern Hebei and the northern
548 NCP, and the MLHs between these two areas were nearly identical.

549 The lower MLH and WS in southern Hebei restricted the atmospheric
550 environmental capability and the pollutant dissipation ability, respectively.
551 Accompanied by higher RH values (stronger pollutant growth ability), the adverse
552 weather conditions will cause severe haze to occur easily in southern Hebei, and the
553 industrial layout in the NCP is in need of restructuring. Heavily polluting enterprises
554 should be relocated to locations with better weather conditions (e.g., some northern
555 areas and coastal areas), and strong emission reduction measures should be
556 implemented in the remaining industrial enterprises to improve air quality.

557 Overall, the present study is the first to conduct a long-term observation of the
558 MLH with high spatial and temporal resolution on a regional scale. The observation
559 results will be of great importance for model parameterization scheme promotion and
560 provide basic information for the distribution of weather conditions in the NCP region.
561 The deficiency of this study is that we did not account for the transport effect on
562 $PM_{2.5}$ concentrations. Because pollutants are usually transported from south to north
563 in the NCP region during haze episodes (Zhu et al., 2016; Tang et al., 2015), pollutant
564 transport has a greater impact on the northern areas and has less influence on the
565 results of this analysis. The absence of sounding data at noon is another shortcoming,
566 and the daytime observations will be implemented in future experiments.
567 Nevertheless, our study can provide reasonable and scientific suggestions for
568 industrial layout and air pollution emission reduction measures for the NCP region,
569 which will be of great importance for achieving the integrated development goals.

570 **Acknowledgments**

571 This work was supported by the National Key R&D Program of China
572 (2017YFC0210000), the National Natural Science Foundation of China (41705113),
573 the Beijing Municipal Science and Technology Project (ZL171100000617002) and
574 the National Earth System Science Data Sharing Infrastructure, National Science &
575 Technology Infrastructure of China.

576 **References**

577
578 Alexander, G., M. Wiegner, B. Bonn, K. Schäfer, R. Forkel, E. Schneidemesser, C.
579 Münkel, K. Chan, and R. Nothard: Mixing layer height as an indicator for urban

582 air quality? *Atmos. Meas. Tech.*, 10, 2969-2988,
583 doi.org/10.5194/amt-10-2969-2017, 2017.

584 Beyrich, F.: Mixing height estimation from SODAR data – a critical discussion,
585 *Atmos. Environ.*, 31, 3941–3953, 1997.

586 Bond, T., S. Doherty, D. Faherty et al.: Bounding the role of black carbon in the
587 climate system: a scientific assessment, *J. Geophys. Res.*, 118, 1-173,
588 doi:10.1002/jgrd.50171, 2013.

589 Chen, W., H. Kuze, A. Uchiyama, Y. Suzuki, and N. Takeuchi: One-year observation
590 of urban mixed layer characteristics at Tsukuba, Japan using a micro pulse lidar,
591 *Atmos. Environ.*, 35, 4273–4280, doi:10.1016/S1352-2310(01)00181-9, 2001.

592 Emeis, S., C. Münkel, S. Vogt, W. Müller, and K. Schäfer: Atmospheric
593 boundary-layer structure from simultaneous SODAR, RASS, and ceilometer
594 measurements, *Atmos. Environ.*, 38(2), 273-286,
595 doi:10.1016/j.atmosenv.2003.09.054, 2004.

596 Emeis, S., K. Schäfer, and C. Münkel: Observation of the structure of the urban
597 boundary layer with different ceilometers and validation by RASS data,
598 *Meteorologische Zeitschrift*, 18(2), 149-154, doi:10.1127/0941-2948/2009/0365,
599 2009.

600 Emeis, S., K. Schäfer, C. Münkel, R. Friedl, and P. Suppan: Evaluation of the
601 Interpretation of Ceilometer Data with RASS and Radiosonde Data, *Bound.-Lay.*
602 *Meteorol.*, 143(1), 25-35, doi:10.1007/s10546-011-9604-6, 2011.

603 Eresmaa, N., A. Karppinen, S. Joffre, J. Räsänen, and H. Talvitie: Mixing height
604 determination by ceilometer, *Atmos. Chem. Phys.*, 6, 1485–1493, doi:
605 10.5194/acp-6-1485-2006, 2006.

606 Fu, G., W. Xu, R. Yang, J. Li, and C. Zhao: The distribution and trends of fog and
607 haze in the North China Plain over the past 30 years, *Atmos. Chem. Phys.*, 14
608 (21), 11949-11958, 2014.

609 Garratt, J.: The atmospheric boundary layer. Cambridge University Press, U.K., 316,
610 1994.

611 Guo, J., Y. Miao, Y. Zhang, H. Liu, Z. Li, W. Zhang, J. He, M. Lou, Y. Yan, L. Bian,
612 and P. Zhai: The climatology of planetary boundary layer height in China derived
613 from radiosonde and reanalysis data, *Atmos. Chem. Phys.*, 16(20), 13309-13319,
614 doi:10.5194/acp-16-13309-2016, 2016.

615 Guo, J., X. Zhang, Y. Wu, H. Che, Laba, and X. Li: Spatio-temporal variation trends
616 of satellite-based aerosol optical depth in China during 1980-2008, *Atmos.*
617 *Environ.*, 45(37), 6802-6811, doi: 10.1016/j.atmosenv.2011.03.068, 2011.

618 He, Q. and Mao, J.: Observation of urban mixed layer at Beijing using a micro pulse
619 lidar, *Acta Meteorol. Sin.*, 63, 374–384, 2005.

620 Hu, M., S. Liu, Z. Wu, J. Zhang, Y. Zhao, W. Birgit, and W. Alfred: Effects of high
621 temperature, high relative humidity and rain process on particle size distributions
622 in the summer of Beijing, *Environ. Sci.*, 27(11), 2006.

623 Hu, X., Z. Ma, W. Lin, H. Zhang, J. Hu, Y. Wang, X. Xu, J. Fuentes, and M. Xue:
624 Impact of the Loess Plateau on the atmospheric boundary layer structure and air
625 quality in the North China Plain?: A case study, *Sci. Total Environ.*, 499,

626 228–237, doi:10.1016/j.scitotenv.2014.08.053, 2014.

627 Jacobson, M.: Strong radiative heating due to the mixing state of black carbon in
628 atmospheric aerosols, *Nature*, 409, 695–697, 2001.

629 Ji, D., Y. Wang, L. Wang, L. Chen, B. Hu, G. Tang, J. Xin, T. Song, T. Wen, Y. Sun, Y.
630 Pan, Z. Liu: Analysis of heavy pollution episodes in selected cities of northern
631 China, *Atmos. Environ.*, 50(2012), 338–348, 2012.

632 Li, M., G. Tang, J. Huang, Z. Liu, J. An, and Y. Wang: Relationship between
633 atmospheric MLH and winter haze pollution in the Jing-Jin-Ji region, *Environ.*
634 *Sci.*, 2015,(06):1935–1943, 2015.

635 Li, P., J. Xin, X. Bai, Y. Wang, S. Wang, S. Liu, and X. Feng: Observational studies
636 and a statistical early warning of surface ozone pollution in Tangshan, the largest
637 heavy industry city of North China, *Inter. J. Env. Res. Pub. Heal.*, 10(3),
638 1048–1061, doi:10.3390/ijerph10031048, 2013.

639 Li, Z., W. Lau, and V. Ramanathan et al.: Aeolosol and monsoon climate interactions
640 over Asia, *Rev. Geophys.*, 54, 886–929, doi:10.1002/2015RG000500, 2016.

641 Liu, Z., Y. Sun, L. Li and Y. Wang: Particle mass concentrations and size distribution
642 during and after the Beijing Olympic Games, *Environ. Sci.*, 32(4),
643 doi:10.13227/j.hjxk.2011.04.015, 2011.

644 Liu, Z., B. Hu, J. Zhang, Y. Yu, and Y. Wang: Characteristics of aerosol size
645 distributions and chemical compositions during wintertime pollution episodes in
646 Beijing, *Atmos. Res.*, 168, 1–12, doi:10.1016/j.atmosres.2015.08.013, 2016.

647 Miao, Y., X. Hu, S. Liu, T. Qian, M. Xue, Y. Zheng, and S. Wang: Seasonal variation
648 of local atmospheric circulations and boundary layer structure in the
649 Beijing-Tianjin-Hebei region and implications for air quality, *J. Adv. Model.*
650 *Earth. Sy.*, 7(4), 1602–1626, doi:10.1002/2015ms000522, 2015.

651 Münkel, C., and J. Räsänen: New optical concept for commercial lidar ceilometers
652 scanning the boundary layer, *P.SPIE*, 5571, 364–374, 2004.

653 Münkel, C., N. Eresmaa, J. Räsänen, and A. Karppinen: Retrieval of mixing height
654 and dust concentration with lidar ceilometer, *Bound.-Lay. Meteorol.*, 124(1),
655 117–128, doi:10.1007/s10546-006-9103-3, 2007.

656 Muñoz, R., and A. Undurraga: Daytime Mixing layer over the Santiago Basin:
657 Description of Two Years of Observations with a Lidar Ceilometer, *J. Appl.*
658 *Meteorol. Clim.*, 49(8), 1728–1741, doi:10.1175/2010jamc2347.1, 2010.

659 Peng, J., M. Hu, S. Guo, Z. Du, J. Zheng, D. Shang, M. Zamora, L. Zeng, M. Shao, Y.
660 Wu, J. Zheng, Y. Wang, C. Glen, D. Collins, M. Molina, and R. Zhang: Markedly
661 enhanced absorption and direct radiative forcing of black carbon under polluted
662 urban environments, *P. Natl. Acad. Sci. Usa.*, 113(4266–4271),
663 doi:10.1073/pnas.1602310113, 2016.

664 Puygrenier, V., F. Lohou, B. Campistron, F. Saïd, G. Pigeon, B. Bénech, and D. Serça:
665 Investigation on the fine structure of sea-breeze during ESCOMPTE experiment,
666 *Atmos. Res.*, 74(1–4), 329–353,
667 doi:<http://dx.doi.org/10.1016/j.atmosres.2004.06.011>, 2005.

668 Quan, J., Y. Gao, Q. Zhang, X. Tie, J. Cao, S. Han, J. Meng, P. Chen, and D. Zhao:
669 Evolution of planetary boundary layer under different weather conditions, and its

670 impact on aerosol concentrations, *Particuology*, 11, 34–40,
671 doi:10.1016/j.partic.2012.04.005, 2013.

672 Schween, J., A. Hirsikko, U. Löhner, and S. Crewell: Mixing-layer height retrieval
673 with ceilometer and Doppler lidar: from case studies to long-term assessment,
674 *Atmos. Meas. Tech.*, 7(11), 3685–3704, doi:10.5194/amt-7-3685-2014, 2014.

675 Seibert, P., F. Beyrich, S. Gryning, S. Joffre, A. Rasmussen, and P. Tercier: Review
676 and intercomparison of operational methods for the determination of the mixing
677 height, *Atmos. Environ.*, 34(7), 1001–1027,
678 doi:[http://dx.doi.org/10.1016/S1352-2310\(99\)00349-0](http://dx.doi.org/10.1016/S1352-2310(99)00349-0), 2000.

679 Seidel, D., C. Ao, and K. Li: Estimating climatological planetary boundary layer
680 heights from radiosonde observations: Comparison of methods and uncertainty
681 analysis, *J. Geophys. Res.*, 115, D16113, doi:10.1029/2009JD013680, 2010.

682 Seinfeld, J. and S. Pandis: *Atmospheric Chemistry and Physics: From Air Pollution to
683 Climate Change*, New York: John Wiley and Sons, 1998.

684 Sicard, M., C. Pérez, F. Rocadenbosch, J. Baldasano, and D. García-Vizcaino:
685 Mixed-Layer Depth Determination in the Barcelona Coastal Area From Regular
686 Lidar Measurements: Methods, Results and Limitations. *Boundary-Layer
687 Meteorology* 119, 135–157, 2006.

688 Sokół, P., I. Stachlewska, I. Ungureanu, and S. Stefan: Evaluation of the boundary
689 layer morning transition using the CL-31 ceilometer signals, *Acta Geophys.*,
690 62(2), doi:10.2478/s11600-013-0158-5, 2014.

691 Stull, R.: *An Introduction to Boundary Layer Meteorology*, Kluwer Academic
692 Publishers, Dordrecht, 1988.

693 Su, F., M. Yang, J. Zhong, Z. Zhang: The effects of synoptic type on regional
694 atmospheric contamination in North China, *Res. Of Environ. Sci.*, 17(3),
695 doi:10.13198/j.res.2004.03.18.sufq.006, 2004.

696 Tang, G., J. Zhang, X. Zhu, T. Song, C. Münkel, B. Hu, K. Schäfer, Z. Liu, J. Zhang,
697 L. Wang, J. Xin, P. Suppan, and Y. Wang: Mixing layer height and its
698 implications for air pollution over Beijing, China, *Atmos. Chem. Phys.*, 16(4),
699 2459–2475, doi:10.5194/acp-16-2459-2016, 2016.

700 Tang, G., P. Zhao, Y. Wang, W. Gao, M. Cheng, J. Xin, X. Li, Y. Wang: Mortality and
701 air pollution in Beijing: the long-term relationship. *Atmos. Environ.*, 150,
702 238–243, doi: 10.1016/j.atmosenv.2016.11.045, 2017a.

703 Tang, G., X. Li, Y. Wang, J. Xin, and X. Ren: Surface ozone trend details and
704 interpretations in Beijing, 2001–2006, *Atmos. Chem. Phys.*, 9, 8813–8823,
705 doi:10.5194/acp-9-8813-2009, 2009.

706 Tang, G., X. Zhu, B. Hu, J. Xin, L. Wang, C. Münkel, G. Mao, and Y. Wang: Impact
707 of emission controls on air quality in Beijing during APEC 2014: lidar ceilometer
708 observations, *Atmos. Chem. Phys.*, 15(21), 12667–12680,
709 doi:10.5194/acp-15-12667-2015, 2015.

710 Tang, G., X. Zhu, J. Xin, B. Hu, T. Song, Y. Sun, J. Zhang, L. Wang, M. Cheng, N.
711 Chao, L. Kong, X. Li, Y. Wang. Modelling study of boundary-layer ozone over
712 northern China - Part I: Ozone budget in summer. *Atmos. Res.*, 187, 128–137,
713 2017b.

714 Tang, G., Y. Wang, X. Li, D. Ji, S. Hsu, and X. Gao: Spatial-temporal variations in
715 surface ozone in Northern China as observed during 2009–2010 and possible
716 implications for future air quality control strategies, *Atmos. Chem. Phys.*, 12,
717 2757-2776, doi:10.5194/acp-12-2757-2012, 2012.

718 Tomasi, F., M. Miglietta, and M. Perrone: The Growth of the Planetary Boundary
719 Layer at a Coastal Site: a Case Study, *Bound.-Lay. Meteorol.*, 139:521-541, doi:
720 10.1007/s10546-011-9592-6, 2011.

721 Tu, J., S. Zhang, X. Cheng, W. Yang, and Y. Yang: Temporal and Spatial Variation of
722 Atmospheric Boundary Layer Height(ABLH) over the Yellow East China Sea, *J.
723 Ocean U. China*, 42(4):7-18, 2012.

724 Kamp, V., and I. McKendry: Diurnal and Seasonal Trends in Convective Mixed-Layer
725 Heights Estimated from Two Years of Continuous Ceilometer Observations in
726 Vancouver, BC, *Bound.-Lay. Meteorol.*, 137(3), 459-475,
727 doi:10.1007/s10546-010-9535-7, 2010.

728 Nair, V., K. Moorthy, D. Alappattu, P. Kunhikrishnan, S. George, P. Nair, S. Babu, B.
729 Abish, S. Satheesh, S. Tripathi, K. Niranjan, B. Madhavan, V. Srikant, C. Dutt, K.
730 Badarinath, and R. Reddy: Wintertime aerosol characteristics over the
731 Indo-Gangetic Plain (IGP): Impacts of local boundary layer processes and
732 long-rang transport, *J. Geo. Res.*: 2006JD008099, doi:10.1029/2006JD008099,
733 2007.

734 Wagner, M., S. Emeis, V. Freudenthaler, B. Heese, W. Junkermann, C. Münkel, K.
735 Schäfer, M. Seefeldner, and S. Vogt: Mixing layer height over Munich, Germany:
736 Variability and comparisons of different methodologies, *J. Geophys. Res.*, 111,
737 D13201, doi:10.1029/2005JD006593, 2006.

738 Wagner, P., and K. Schäfer: Influence of mixing layer height on air pollutant
739 concentrations in an urban street canyon, *Urban Climate*,
740 <http://dx.doi.org/10.1016/j.uclim.2015.11.001>, 2015.

741 Wang, L., N. Zhang, Z. Liu, Y. Sun, D. Ji, and Y. Wang: The Influence of Climate
742 Factors, Meteorological Conditions, and Boundary-Layer Structure on Severe
743 Haze Pollution in the Beijing-Tianjin-Hebei Region during January 2013, *Adv.
744 Meteorol.*, 2014, 1-14, doi:10.1155/2014/685971, 2014.

745 Wang, Y., L. Yao, L. Wang, Z. Liu, D. Ji, G. Tang, J. Zhang, Y. Sun, B. Hu, and J. Xin:
746 Mechanism for the formation of the January 2013 heavy haze pollution episode
747 over central and eastern China, *Sci. China Earth Sci.*, 57(1), 14-25,
748 doi:10.1007/s11430-013-4773-4, 2013a.

749 Wang, Y., M. Zamora, and R. Zhang: New Directions: Light absorbing aersols and
750 their atmospheric impacts, *Atmos. Environ.*, 81, 713-715, doi:
751 10.1016/j.atmosenv.2013.09.034, 2013b.

752 Wei, J., G. Tang, X. Zhu, L. Wang, Z. Liu, M. Cheng, C. Münkel, X. Li, and Y. Wang:
753 Thermal internal boundary layer and its effects on air pollutants during summer
754 in a coastal city in North China, *Journal of Environmental Sciences*, 1001-0742,
755 doi:10.1016/j.jes.2017.11.006, 2017.

756 Wiegner, M., F. Madonna, I. Binietoglou, R. Forkel, J. Gasteiger, A. Geiß, G.
757 Pappalardo, K. Schäfer, and W. Thomas: What is the benefit of ceilometers for

758 aerosol remote sensing? An answer from ERALINET, *Atmos. Meas. Tech.*, 7,
759 1979-1997, doi: 10.5194/amt-7-1979-2014, 2014.

760 Xu, R., G. Tang, Y. Wang, and X. Tie: Analysis of a long-term measurement of air
761 pollutants (2007-2011) in North China Plain (NCP); Impact of emission
762 reduction during the Beijing Olympic Games, *Chemosphere*, 159, 647-658,
763 doi:10.1016/j.chemosphere.2016.06.025, 2016.

764 Yu, H., S. Liu, and R. Dickinson: Radiative effects of aerosols on the evolution of the
765 atmospheric boundary layer, *J. Geo. Res.: Atmos.*, 107, D12(4142),
766 doi:10.1029/2001JD000754, 2002.

767 Zhang, Z., X. Cai, Y. Song, L. Kang, X. Huang, and Q. Li: Temporal and spatial
768 variation of atmospheric boundary layer height over Hainan Island and its
769 adjacent sea areas, *Acta. Sci. Nat. Univ. Pekin.*, 49:83-90, doi:
770 10.13209/j.0479-8023.2013.105, 2013.

771 Zhang, H., Y. Wang, J. Hu, Q. Ying, and X. Hu: Relationships between meteorological
772 parameters and criteria air pollutants in three megacities in China, *Environ. Res.*,
773 140, 242–254, doi:10.1016/j.envres.2015.04.004, 2015a.

774 Zhang, J., Y. Sun, Z. Liu, D. Ji, B. Hu, Q. Liu, and Y. Wang: Characterization of
775 submicron aerosols during a month of serious pollution in Beijing, 2013, *Atmos.*
776 *Chem. Phys.*, 14(6), 2887-2903, doi:10.5194/acp-14-2887-2014, 2014.

777 Zhang, Q., J. Xin, Y. Yin, L. Wang, and Y. Wang: The Variation and Trends of MODIS
778 C5 & C6 Products' Errors in the Recent Decade over the Background and Urban
779 Areas of North China, *Remote Sensing*, 8(9), 754, doi:10.3390/rs8090754,
780 2016b.

781 Zhang, R., G. Hui, S. Guo, M. Zamora, Q. Ying, Y. Lin, W. Wang, M. Hu, and Y.
782 Wang: Formation of Urban Fine Particulate Matter, *Chem. Rev.*, 115, 3803-3855,
783 doi: 10.1021/acs.chemrev.5b00067, 2015b.

784 Zhang, R.: Getting to the Critical Nucleus of Aerosol Formation, *Science*, 328(5984),
785 1366-1367, doi: 10.1126/science.1189732, 2010.

786 Zhang, W., J. Guo, Y. Miao, H. Liu, Y. Zhang, Z. Li, and P. Zhai: Planetary boundary
787 layer height from CALIOP compared to radiosonde over China, *Atmos. Chem.*
788 *Phys.*, 16, 9951–9963, doi: 10.5194/acp-16-9951-2016, 2016a.

789 Zhao, X., P. Zhao, J. Xu, W. Meng, W. Pu, F. Dong, D. He, and Q. Shi: Analysis of a
790 winter regional haze event and its formation mechanism in the North China Plain,
791 *Atmos. Chem. Phys.*, 13 (11), 5685-5696, 2013.

792 Zhu, X., G. Tang, B. Hu, L. Wang, J. Xin, J. Zhang, Z. Liu, C. Münkel, and Y. Wang:
793 Regional pollution and its formation mechanism over North China Plain: A case
794 study with ceilometer observations and model simulations, *J. Geo. Res.: Atmos.*,
795 2016JD025730, doi:10.1002/2016JD025730, 2016.

796

797

798

799

800

801

802

803